

SSUMamba: Spatial-Spectral Selective State Space Model for Hyperspectral Image Denoising

Guanyiman Fu, Fengchao Xiong, *Member, IEEE*, Jianfeng Lu, *Member, IEEE*, Jun Zhou, *Senior Member, IEEE*, and Yuntao Qian, *Senior Member, IEEE*

Abstract—Denoising hyperspectral images (HSIs) is a crucial preprocessing procedure due to the noise originating from intra-imaging mechanisms and environmental factors. Utilizing domain-specific knowledge of HSIs, such as spectral correlation, spatial self-similarity, and spatial-spectral correlation, is essential for deep learning-based denoising. Existing methods are often constrained by running time, space complexity, and computational complexity, employing strategies that explore these priors separately. While these strategies can avoid some redundant information, they inevitably overlook broader and more underlying long-range spatial-spectral information that positively impacts image restoration. This paper proposes a Spatial-Spectral Selective State Space Model-based U-shaped network, termed Spatial-Spectral U-Mamba (SSUMamba), for hyperspectral image denoising. We can obtain complete global spatial-spectral correlation within a module thanks to the linear space complexity in State Space Model (SSM) computations. We introduce a Spatial-Spectral Alternating Scan (SSAS) strategy for HSIs, which helps model the information flow in multiple directions in 3-D HSIs. Experimental results demonstrate that our method outperforms compared methods. The source code will be available at <https://github.com/Ironkitty/SSUMamba>.

Index terms— Hyperspectral image denoising, selective state space model, mamba, global spatial-spectral correlation, deep learning

I. INTRODUCTION

Hyperspectral images (HSIs) provide not only spatial but also detailed material information through the continuous spectral bands they capture. HSIs have been extensively used in material recognition [1], object detection [2]–[4], object tracking [5], [6], change detection [7], and environment protection [8]. During the acquisition of hyperspectral data, various factors such as insufficient exposure time, mechanical vibrations of imaging platforms, atmospheric perturbations, stochastic errors in photon counting, and other intrinsic and extrinsic elements inevitably introduce noise to the images [9], [10]. This noise interferes with the interpretation and application of HSIs. Therefore, HSI denoising becomes an essential preprocessing step to enhance image quality and practical value for various high-level computer vision tasks.

Deep learning-based denoising methods have recently garnered undivided attention. By leveraging data-driven learning, these methods can learn the 3-D nature of HSIs with spectral and spatial information. Due to the challenges posed by the design of methodology, running time, and spatial and computational complexity, existing deep learning-based methods often decompose this 3-D nature into several distinct domains for exploration, such as spatial self-similarity, spectral correlation, and spatial-spectral correlation. For example, recurrent neural

networks (RNNs) and convolutional neural networks (CNNs) are resort to exploit spectral correlation and spatial-spectral correlation, respectively [11]. Moreover, attention mechanisms are concatenated to CNNs to capture spatial self-similarity further [12]. Transformer-based methods are also employed to capture long-range correlation in HSIs [9], [13], [13]. However, suffering from the $O(n^2)$ complexity of the self-attention mechanism, these methods incorporate multiple modules to explore different domain knowledge, respectively, to reduce the length of tokens and avoid redundant information.

However, given the tri-dimensional nature of HSIs, which demonstrate spatial solid continuity and spectral correlation, it is essential to explore the complete global spatial-spectral correlation, especially in image restoration tasks where detailed information tends to degrade. Broader and more underlying long-range spatial-spectral information has a positive impact that should be considered. The State Space Model (SSM) [14], [15], an approach rooted in control systems, has attracted attention for its linear complexity in handling long input sequences. Recently, Mamba [14], an optimization for SSM, has shown unique advantages in computer vision tasks [16], [17], while its linear complexity should offer promising advantages in global spatial-spectral correlation modeling in HSIs. Liu *et al.* [18] introduced a SSM-based method for HSI denoising to exploit the bidirectional spatial information in HSIs. However, how to apply the SSM to HSIs denoising to capture the global spatial-spectral correlation following the 3-D nature of HSIs remains an open question.

This paper introduces a Spatial-Spectral Selective SSM-based HSI denoising method, Spatial-Spectral U-Mamba (SSUMamba), for HSI denoising. To address the disparity between image data and sequence data, we introduce the Spatial-Spectral Alternating Scan (SSAS) Mamba aimed to improve the exploration of local texture in the data and mitigate the unidirectional dependency issue present in the SSM. Our architecture incorporates a SSAS strategy for HSI data, which helps model the information flow in multiple directions in HSIs. Furthermore, we apply SSAS Mamba block in a U-shape network architecture to exploit multi-scale features and recover the HSI. Thanks to its linear complexity, SSUMamba can explore the complete global spatial-spectral correlation. The SSAS strategy further enhances the 3-D characteristics of HSI. Our SSUMamba demonstrates superior performance compared to other methods. The contributions of this article can be summarized as follows:

- The linear complexity of the Selective State Space Model (SSM) enables the modeling of global spatial-spectral

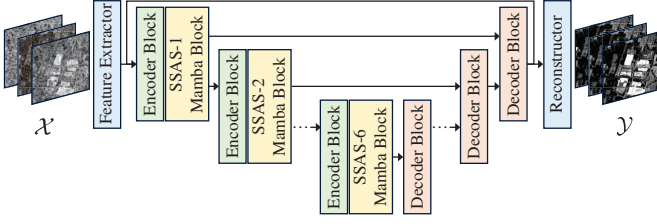


Fig. 1. SSUMamba uses the encoder-decoder framework, incorporating a feature extractor, encoder blocks, Spatial-Spectral Alternating Scan (SSAS) Mamba blocks, decoder blocks with skip connections, and a reconstructor.

flow in cross directions. Shi *et al.* [53] further proposed an omni selective scan mechanism to model information flows to include the feature dimensions. SSM in HSI modeling has been widely explore [54], [55]. Liu *et al.* [18] apply the SSM to HSI denoising to exploit the bidirectional spatial information. However, the application of SSM to exploit the global spatial-spectral correlation in HSIs denoising remains unexplored.

III. METHOD

In this section, we first introduce the preliminaries of SSM and Mamba. Then, we provide a detailed exposition of the proposed SSUMamba, including the overall architecture, the Spatial-Spectral Alternating Scan (SSAS) Mamba block, and the design details.

A. Preliminaries: State Space Models

State Space Models (SSMs) are conceptualized using continuous systems that map a one-dimensional sequence $x(t) \in \mathbb{R}^L$ to the output response $y(t) \in \mathbb{R}^M$. The SSM is defined by the following ordinary differential equation (ODE):

$$\begin{aligned} h'(t) &= Ah(t) + Bx(t) \\ y(t) &= Ch(t) + Dx(t) \end{aligned} \quad (1)$$

where $h(t) \in \mathbb{R}^N$ is the hidden state, $A \in \mathbb{R}^{N \times N}$, $B \in \mathbb{R}^{N \times L}$, $C \in \mathbb{R}^{M \times N}$, and $D \in \mathbb{R}^{M \times L}$ are the parameters of the SSM. The hidden state $h(t)$ is updated by the input $x(t)$ and the previous hidden state $h(t-1)$, and the output $y(t)$ is generated by the hidden state $h(t)$ and the input $x(t)$.

Following [15], we consider the case of a single-input single-output system, where $L = M = 1$, and omit the $Dx(t)$ term. The ODE in Eq. (1) can be discretized using the zeroth-order hold (ZOH) as follows:

$$\begin{aligned} h_t &= \bar{A}h_{t-1} + \bar{B}x_t \\ y_t &= \bar{C}h_t \end{aligned} \quad (2)$$

where \bar{A}, \bar{B} are discrete parameters from A, B as follows:

$$\begin{aligned} \bar{A} &= e^{\Delta A} \\ \bar{B} &= (\Delta A)^{-1}(e^{\Delta A} - I) \cdot \Delta B \end{aligned} \quad (3)$$

where Δ is sampling step.

As we can see Eq. (2) can be computed similarly to RNNs. To further accelerate the computation, Gu *et al* [15] unroll the computation of the SSM into a convolution formulated as follows:

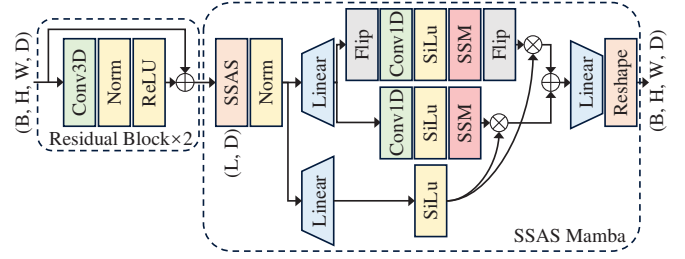


Fig. 2. The introduced SSAS Mamba block, which contains residual blocks and a SSAS Mamba layer.

$$y = x * \bar{K} \quad (4)$$

where $\bar{K} = (C\bar{B}, C\bar{A}\bar{B}, C\bar{A}^2\bar{B}, \dots, C\bar{A}^{k-1}\bar{B})$ is the kernel of the convolution, $*$ denotes the convolution operation, and k is the sequence length of input.

In Eq (2), parameters are fixed within all time steps. Gu *et al* [14] introduce a method to optimize the parameters of SSM in a selective scan mechanism. The parameters $\bar{B}, \bar{C} \in \mathbb{R}^{L \times N}$ and $\Delta \in \mathbb{R}^{L \times D}$ are learned from input data $x \in \mathbb{R}^{L \times D}$ and output data $y \in \mathbb{R}^{L \times D}$, L is a length dimension, D and N are numbers of channel. Gu *et al* [14] also propose hardware-aware optimization to ensure its efficient implementation.

In this paper, we follow the Mamba framework proposed in [14] and apply it to spatial-spectral modeling processing.

B. Overview Architecture

To model the global spatial-spectral correlation and enhance the 3-D characteristics of HSIs in denoising, we propose the SSUMamba, as shown in Fig. 1. Let $\mathcal{Y} \in \mathbb{R}^{B \times H \times W}$ be a clean HSI with $H \times W$ pixels and B bands. When subjected to additive noises \mathcal{E} , such as Gaussian noise, impulse noise, stripes, and deadlines, the observed HSI \mathcal{X} can be mathematically represented as:

$$\mathcal{X} = \mathcal{Y} + \mathcal{E} \quad (5)$$

The Proposed SSUMamba is designed to learn the mapping from \mathcal{X} to \mathcal{Y} for denoising in a U-shaped architecture, including a feature extractor, encoder blocks, Spatial-Spectral Alternating Scan (SSAS) Mamba blocks, decoder blocks, a reconstructor. The feature extractor and reconstructor are utilized to extract HSI features with a shape of (B, H, W, D) , where D represents the number of channels, and to recover the HSI from the features, respectively. The encoder blocks employ downsampling and 3-D convolutions to extract multi-scale features from the observed HSI feature in multi-scale, while the SSAS Mamba block are employed to model the local texture and global spatial-spectral correlation. The decoder blocks use upsampling and 3-D convolutions to reconstruct the features extracted by the encoder blocks and SSAS Mamba blocks.

C. Spatial-Spectral Alternating Scan Mamba Block

The Mamba model [14] shows compelling characteristics in achieving global receptive fields, dynamic weights, and

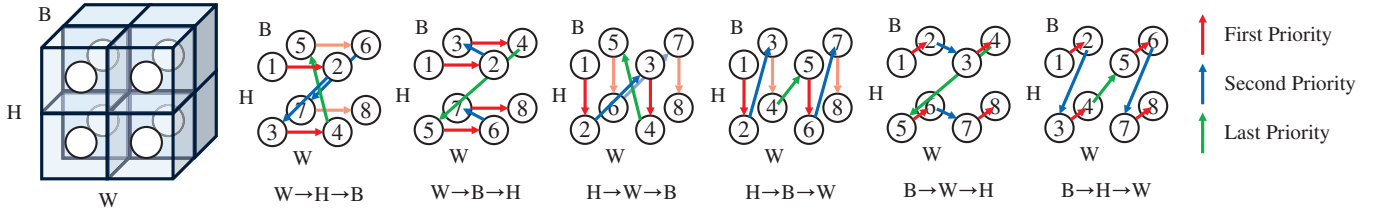


Fig. 3. The Spatial-Spectral Alternating Scan (SSAS) includes 6 variants when processing 3-D data with a shape of $2 \times 2 \times 2$. The scanning process within each pixel adheres to a specific priority. For example, in the variant “ $W \rightarrow H \rightarrow B$ ”, the processing scans the W direction until there are no pixels in that direction, then proceeds to scan the next line in $H + 1$, and finally in $B + 1$.

linear computational complexity. While the sequential nature of Mamba fits well with NLP tasks involving temporal data, it presents significant challenges when applied to HSI data, which is non-sequential and has strong spatial continuity and spectral correlation. To address this issue, we introduce a Spatial-Spectral Alternating Scan (SSAS) Mamba block for HSI modeling, as shown in Fig. 2. The SSAS Mamba block consists of Residual Blocks and a SSAS Mamba layer.

Unlike the sequence data, vision data is rich in spatial information [51]. Additionally, HSIs feature strong local spatial-spectral correlation. In our SSAS Mamba Block, residual blocks with 3-D convolution, Instance Normalization, and Leaky ReLU are applied to the feature to model the local spatial-spectral correlation to enhance the local texture exploration in the SSAS Mamba block.

Moreover, the SSM models all tokens sequentially. However, in non-sequential vision data, the correlation among pixels is in more directions [16], [51]. For example, in vision data, a 2-D selective scan [16] is proposed to exploit the 2-D image in 4 directions: H forward scan, H backward scan, W forward scan, and W backward scan. Considering that HSIs are 3-D data with strong spatial continuity and spectral correlation, information flows are expected in both spatial and spectral dimensions to model global spatial-spectral correlation. Thus, we introduce a Spatial-Spectral Alternating Scan (SSAS) strategy, as shown in Fig. 3, to fully exploit the information flow in all directions. The SSAS include 6 variants with different scanning priorities: $W \rightarrow H \rightarrow B$, $W \rightarrow B \rightarrow H$, $H \rightarrow W \rightarrow B$, $H \rightarrow B \rightarrow W$, $B \rightarrow W \rightarrow H$, and $B \rightarrow H \rightarrow W$, where B , H , and W represent the band, height, and width of the HSI, respectively. The first 4 variants will pay attention to information in spatial dimension, while the last two variants focus on spectral correlation. In each variant, the processing scans all pixels in the first direction and then proceeds to scan the next line in the second and third directions. We incorporate one of the variants of SSAS after the residual blocks and flatten the input HSI feature with the shape of (B, H, W, D) into (L, D) , where $L = B \times H \times W$, to make the block scan in a specific priority. Finally, in our SSUMamba, we use 6 SSAS Mamba blocks with all the 6 variants of SSAS to accomplish the modeling in all directions in HSIs.

Thanks to SSAS, Mamba blocks can model the information flow in different priorities to model the 3-D characteristic of HSI. However, these information flows always sequence from the first pixel (1 in Fig. 3) to the last pixel (8 in Fig. 3). We further introduce a bidirectional Mamba layer to enhance

the information flow. The feature from SSAS will be divided into two parts, one is processed in the forward direction, and the other is processed in the backward direction. After the bidirectional Mamba layer, the SSAS achieves the complete modeling of global spatial-spectral correlation.

D. Architecture Design Details

In the standard setting of our SSUMamba, we incorporate 6 SSAS Mamba blocks with channel set as [32, 64, 64, 128, 128, 256]. The downsampling is enabled in block [2, 4, 6]. The SSUMamba is trained end-to-end to minimize the difference between the predicted clean HSI and the ground truth clean HSI. The loss function is set as:

$$\mathcal{L} = \frac{1}{N} \sum_{i=1}^N \|\hat{\mathcal{Y}}_i - \mathcal{Y}_i\|_F^2 \quad (6)$$

where \mathcal{Y} denotes the HSI recovered from the noisy image \mathcal{X} in SSUMamba, $\hat{\mathcal{Y}}$ denotes the corresponding clean image, and N is the batch size within each iteration. An Adm optimizer with a learning rate of 3×10^{-4} was used to train the SSUMamba model for 45 epochs and decreased with a factor of 0.5 in the 20th and 35th epochs. The batch size is set as 14. The model was implemented using PyTorch and trained on a single NVIDIA GeForce RTX 3090 GPU.

IV. EXPERIMENTS

In this section, we demonstrate the denoising performance of the proposed SSUMamba through synthetic and real-world experiments. Additionally, we conduct further ablation experiments to analyze the performance of each module and varying widths within the network.

A. Experimental Settings

1) *Training and Testing Setting*: In accordance with [11], [33], we opted for 100 HSIs from the Interdisciplinary Computational Vision Laboratory (ICVL) HSI dataset for training. These HSIs were captured using a Specim PS Kappa DX4 hyperspectral camera, sized at 1392×1300 pixels and covering 31 spectral bands ranging from 400 to 700 nm. They were partitioned into patches measuring $64 \times 64 \times 31$ and subjected to augmentation through random flipping, cropping, and resizing. The synthetic datasets include the ICVL testing set, Houston 2018 HSI, and Pavia city center HSI. The real-world datasets comprise the Gaofen-5 (GF-5) Wuhan HSI and

TABLE I
COMPARISON OF DIFFERENT METHODS ON 50 TESTING HSIS FROM ICVL DATASET. THE TOP THREE VALUES ARE MARKED AS **RED**, **BLUE**, AND **GREEN**.

σ	Index	Noisy	Model-based methods								Deep learning-based methods				
			BM4D [25]	MTSNMF [21]	LLRT [27]	NGMeet [28]	LRMR [20]	FastHyDe [29]	LRTFL ₀ [22]	E-3DTV [31]	T3SC [34]	MAC-Net [33]	TRQ3D [13]	SST [9]	SSUMamba (ours)
[0,15]	PSNR \uparrow	33.18	44.39	45.39	45.74	39.63	41.50	48.08	43.41	46.05	49.68	48.21	46.43	50.87	51.47
	SSIM \uparrow	.6168	.9683	.9592	.9657	.8612	.9356	.9917	.9315	.9811	.9912	.9915	.9878	.9938	.9946
	SAM \downarrow	.3368	.0692	.0845	.0832	.2144	.1289	.0404	.0570	.0560	.0486	.0387	.0437	.0298	.0252
[0,55]	PSNR \uparrow	21.72	37.63	38.02	36.80	31.53	31.50	42.86	35.63	40.20	45.15	43.74	44.64	46.39	46.82
	SSIM \uparrow	.2339	.9008	.8586	.8285	.6785	.6233	.9800	.8125	.9505	.9810	.9768	.9840	.9872	.9881
	SAM \downarrow	.7012	.1397	.234	.2316	.4787	.3583	.0630	.1914	.0993	.0652	.0582	.0487	.0457	.0371
[0,95]	PSNR \uparrow	17.43	34.71	34.81	31.89	27.62	27.00	40.84	32.83	37.80	43.10	41.24	43.54	44.83	45.50
	SSIM \uparrow	.1540	.8402	.7997	.6885	.5363	.4208	.9734	.7482	.9279	.9734	.9577	.9806	.9838	.9852
	SAM \downarrow	.8893	.1906	.3266	.3444	.642	.5142	.0771	.3014	.1317	.0747	.0841	.0523	.0513	.0452
Mixture	PSNR \uparrow	13.21	23.36	27.55	18.23	23.61	23.10	27.58	30.93	34.90	34.09	28.44	39.73	39.22	42.76
	SSIM \uparrow	.0841	.4275	.6743	.1731	.4448	.3463	.7250	.8378	.9041	.9052	.7393	.9491	.9626	.9701
	SAM \downarrow	.9124	.5476	.5326	.6873	.6252	.5144	.4534	.3613	.1468	.2340	.4154	.0869	.0743	.0710

the Earth Observing-1 (EO-1) HSI. The number of bands also increases from ICVL to EO-1 HSI, providing a comprehensive evaluation set to test all methods across varying numbers of bands.

2) *Synthetic Data Generation*: As indicated by [56], real-world noises in hyperspectral images (HSIs) typically follow non-independent and identical distribution (non-i.i.d.). Furthermore, remote-sensing HSIs commonly exhibit contamination from a mixture of noises. Hence, in our experiments, we considered non-i.i.d. Gaussian noise and mixture noise. For non-i.i.d. Gaussian noise, we varied the standard deviation within the range of $\sigma \in [0, 15]$, $[0, 55]$, and $[0, 95]$, and $[0, 95]$. The mixture noise comprised the following components: 1) non-i.i.d. Gaussian noise with $\sigma \in [0, 95]$; 2) impulse noise affecting 1/3 of the bands, with intensities spanning from 10% to 70%; 3) strips affecting 5%-15% of columns on 1/3 of the bands; and 4) dead zones affecting 5%-15% of columns on 1/3 of the bands.

3) *Evaluation Index*: To quantitatively assess the denoising performance of all methods, we employed peak signal-to-noise ratio (PSNR), structural similarity (SSIM), and spectral angle mapper (SAM). Higher PSNR and SSIM values, along with smaller SAM values, indicate superior denoising effectiveness.

4) *Compared Methods*: 12 methods were used for comparison, including 8 model-based methods, *i.e.*, BM4D [25], MTSNMF [21], LLRT [27], NGMeet [28], LRMR [20], FastHyDe [29], LRTFL₀ [22], and E-3DTV [31], and 4 deep learning-based methods, *i.e.*, T3SC [34], MAC-Net [33], TRQ3D [13], and SST [9]. For a fair comparison, we retrained one model for all the deep learning-based methods in each noise case.

B. Comparison on Synthetic Datasets

To demonstrate the denoising performance both quantitatively and qualitatively, we first present the denoising results

on the ICVL testing set, Houston 2018, and Pavia city center HSIs.

1) *ICVL testing set*: The ICVL dataset comprises 50 HSIs from the ICVL dataset for synthetic testing. To alleviate the computational burden associated with certain model-based techniques like NGMeet, all these HSIs were resized to $512 \times 512 \times 31$. The ICVL dataset is enriched with a greater number of HSIs, offering a comprehensive evaluation platform to assess the performance of all methods under different noise cases. Thus, both Gaussian and mixture noises were included for assessment. Table I illustrates the quantitative analysis, with the top three results highlighted in bold red, bold blue, and bold green, respectively.

FastHyDe demonstrates superior performance among model-based methods in Gaussian noise cases, attributed to its simultaneous modeling of the GSC and NSS of HSIs. For mixture noise cases, methods like LRTFL₀ and E-3DTV exhibit improved performance. Deep-learning-based approaches leverage their data-driven learning capability, outperforming model-based methods consistently. T3SC and MAC-Net leverage physical modeling and data-driven learning, showcasing robustness against Gaussian noise. Constrained with spectral and spatial transformer-based modules, SST shows the best performance among all compared methods. In summary, SSUMamba stands out as the top performer in all assessed cases. This is attributed to its capability to adeptly capture the domain knowledge of HSIs through global spatial-spectral correlation modeling.

2) *Houston 2018 HSI*: The Houston 2018 HSI was captured using the ITRES CASI hyperspectral imager, comprising 1202×4172 pixels. The Houston HSI contains 48 bands spanning from 380 to 1050 nm. For our experiments, we omit the first 2 bands, which is relatively noisy, and extracted a 512×512 cube from the center of the HSI for synthetic experiments. To replicate real-world noise found in remote-sensing images, we introduced mixture noise to the pristine

TABLE II
COMPARISON OF DIFFERENT METHODS ON HOUSTON 2018 HSI. THE TOP THREE VALUES ARE MARKED AS **RED**, **BLUE**, AND **GREEN**.

Index	Noisy	Model-based methods								Deep learning-based methods				
		BM4D [25]	MTSNMF [21]	LLRT [27]	NGMeet [28]	LRMR [20]	FastHyDe [29]	LRTFL ₀ [22]	E-3DTV [31]	T3SC [34]	MAC-Net [33]	TRQ3D [13]	SST [9]	SSUMamba (ours)
PSNR \uparrow	11.72	22.76	25.86	15.58	22.36	21.84	27.07	28.75	30.64	29.84	28.83	32.55	31.07	34.55
SSIM \uparrow	.0843	.4762	.6933	.1386	.5169	.3914	.7757	.8038	.8570	.8751	.7963	.9194	.9166	.9444
SAM \downarrow	.9778	.5168	.4977	.7652	.5728	.4857	.4518	.2221	.1323	.1943	.2356	.1241	.1390	.1047

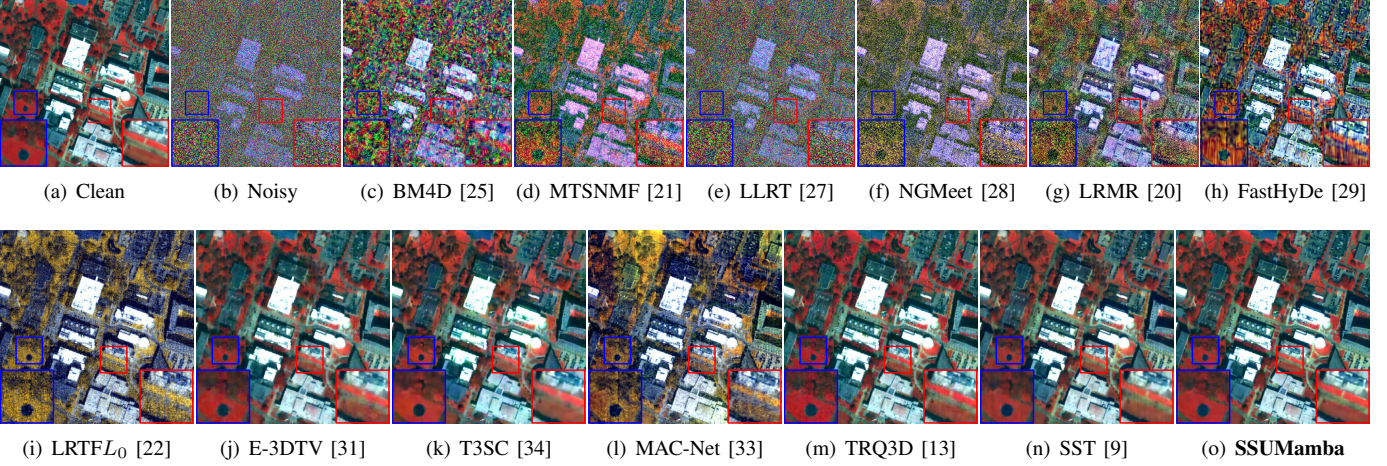


Fig. 4. Denoising results on the Houston 2018 HSI with the mixture noise. The false-color images are generated by combining bands 35, 20, and 5.

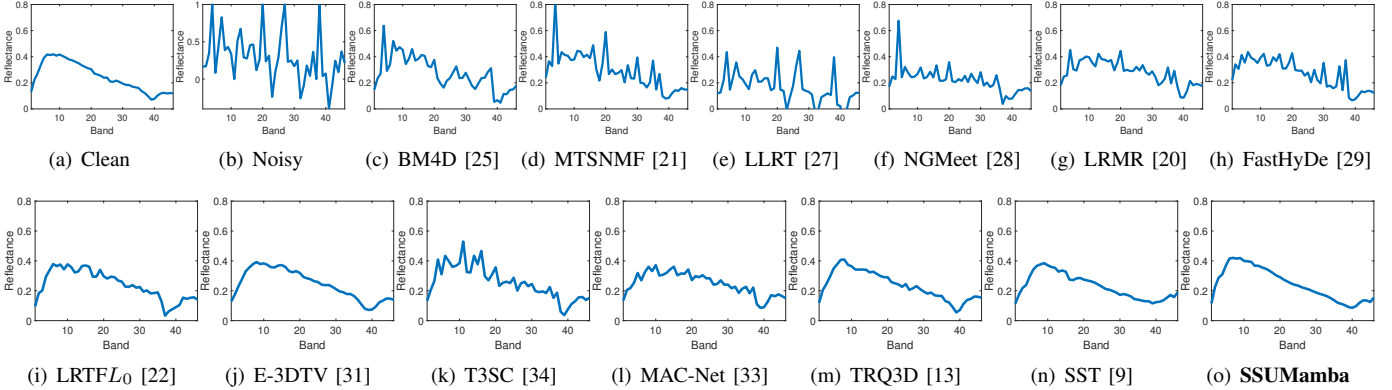


Fig. 5. Reflectance of pixel (380,198) in the Houston 2018 HSI.

HSI, resulting in a noisy HSI. Deep learning models trained on the ICVL dataset were then employed for evaluation. However, it is noteworthy that T3SC, TRQ3D, and SST encounter challenges when dealing with HSIs that feature a distinct number of bands compared to the training data. To mitigate this issue, for T3SC, TRQ3D, and SST, we partitioned the provided HSI into multiple sub-images, each containing 31 bands for testing.

The denoising results are showcased in Table II. All deep learning-based methods learn the mixture noise cases in the ICVL dataset and perform better than model-based methods. However, given the substantial divergence between the Houston 2018 HSI and the training set ICVL, deep learning-based techniques face a formidable challenge when tasked with denoising and exhibiting a decline in performance. Our proposed SSUMamba, despite experiencing some performance

degradation in instances of significant data discrepancies, still outperforms transformer-based approaches.

Fig. 4 illustrates the false-color images recovered from all compared methods. While conventional model-based approaches, tailored for Gaussian noise, struggle with eliminating artifacts such as stripes and artifacts, E-3DTV stands out by employing the l_1 -norm for noise in the mixture noise. Due to spectral variations between the Houston HSI and the ICVL training set, TRQ3D and SST transformers exhibit some degree of failure in Houston image reconstruction. TRQ3D retaining Gaussian noise and stripe artifacts. SST exhibits color distortion, indicating inaccuracies in spectral fidelity relative to the original image, thus revealing limitations in accurately modeling spectral correlations. In contrast, our SSUMamba model utilizes alternating scan Mamba blocks to capture global spatial-spectral correlations effectively. Our

TABLE III
COMPARISON OF DIFFERENT METHODS ON PAVIA CITY CENTER HSI. THE TOP THREE VALUES ARE MARKED AS **RED**, **BLUE**, AND **GREEN**.

Index	Noisy	Model-based methods								Deep learning-based methods				
		BM4D [25]	MTSNMF [21]	LLRT [27]	NGMeet [28]	LRMR [20]	FastHyDe [29]	LRTFL ₀ [22]	E-3DTV [31]	T3SC [34]	MAC-Net [33]	TRQ3D [13]	SST [9]	SSUMamba (ours)
PSNR \uparrow	13.46	21.70	25.15	15.44	23.68	22.72	26.78	26.49	30.44	28.69	27.74	28.23	31.87	35.58
SSIM \uparrow	.2181	.5128	.7397	.2760	.7176	.6524	.8361	.8147	.8941	.8656	.8724	.8665	.9234	.9557
SAM \downarrow	.8893	.5297	.4094	.7902	.4760	.3771	.4040	.3703	.1134	.2135	.3222	.1961	.1676	.1055

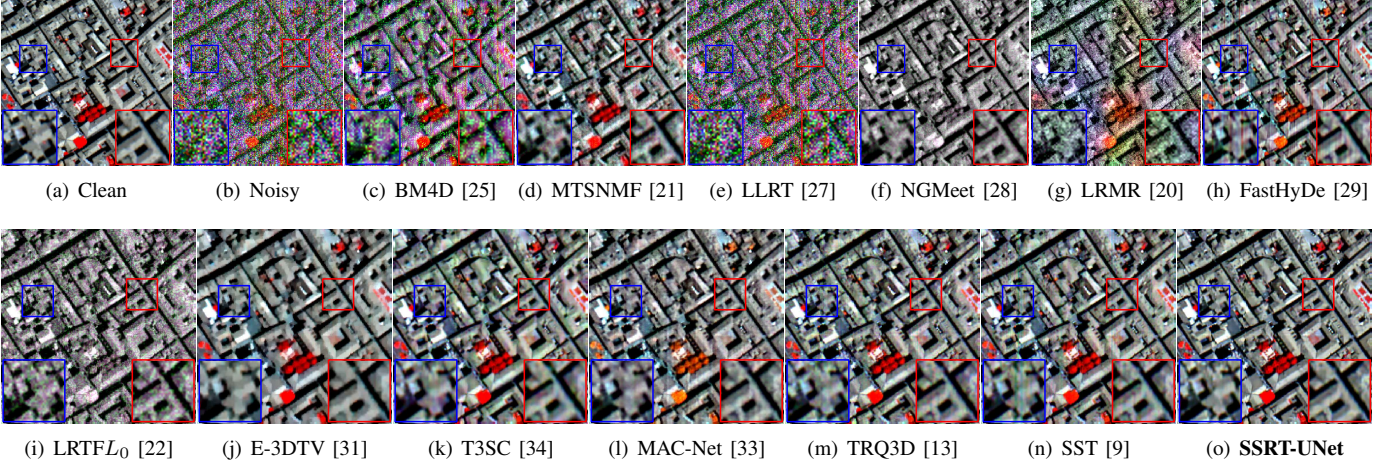


Fig. 6. Denoising results on the Pavia city center HSI with the mixture noise. The false-color images are generated by combining bands 65, 45, and 25.

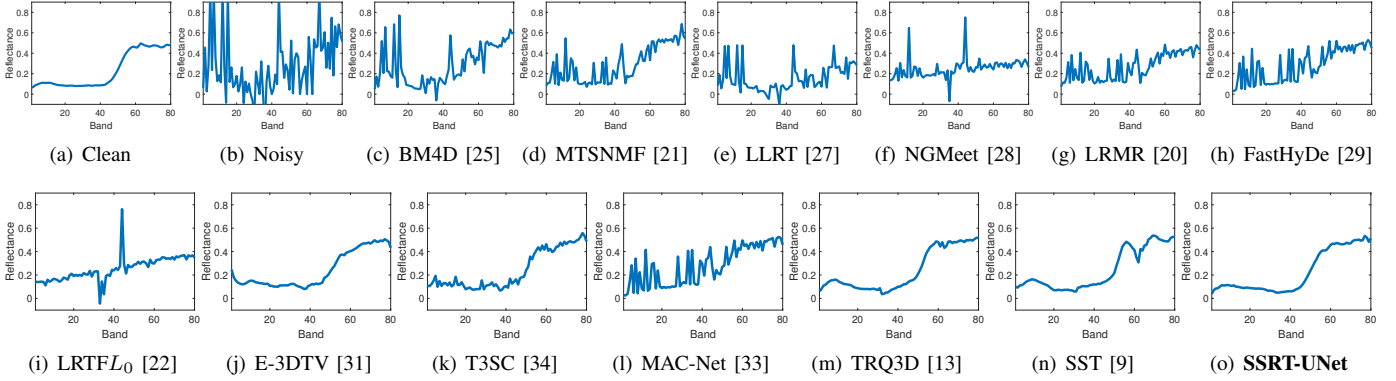


Fig. 7. Reflectance of pixel (170,100) in the Pavia city center HSI.

method yields highly accurate reconstructions with minimal artifacts, particularly in cases with mixture noise, where detailed information degrades. Exploiting long-range spatial-spectral information can help recover degraded data and substantially improve overall performance.

The spectral reflectances are shown in Fig. 5, where the mixture noise makes the spectral distortion drastic, as in Fig. 5(b). Because model-based methods are susceptible to noise type, they struggle to generate recovered spectra that match clean image spectra in denoising mixture noise. Taking into account the mixed noise, E-3DTV models the low-rankness of the spatial and spectral gradient map in HSI, resulting in the best match with the clean HSI among model-based methods. Deep learning-based T3SC and E-3DTV design for Gaussian noise recover the spectral reflectance with jitters. TRQ3D and SST cannot accommodate the processing as the number of bands

in Houston 2018 differs from that in the ICVL training set, resulting in incomplete GSC and less accurate matching of spectral reflectances with clean HSI. Our SSUMamba, with the ability to capture global spatial-spectral correlations, can effectively recover spectral reflectance, demonstrating the best performance in spectral modeling ability among all methods.

3) *Pavia City Center HSI*: The Pavia City Center HSI was captured using the Reflective Optics System Imaging Spectrometer (ROSIS) sensor spanning from 430 to 860 nm. Following [57], we removed the first 22 noisy bands and added mixture noise on a 200×200 subimage with 80 bands for synthetic experiments. Other experimental settings were maintained in line with those used for the Houston 2018 HSI.

Table III shows a quantitative presentation of the results of the experiment. Model-based E-3DTV calculates sparsity on gradient map subspaces across all HSI bands. Its ability

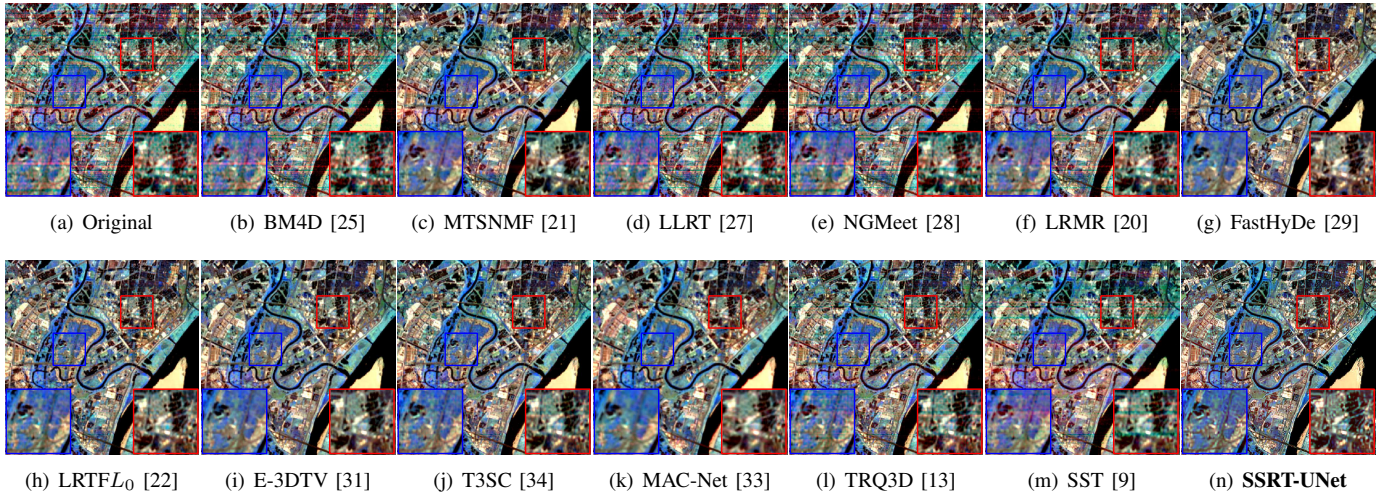


Fig. 8. Denoising results on the GF-5 Wuhan HSI. The false-color images are generated by combining bands 152, 83, and 33.

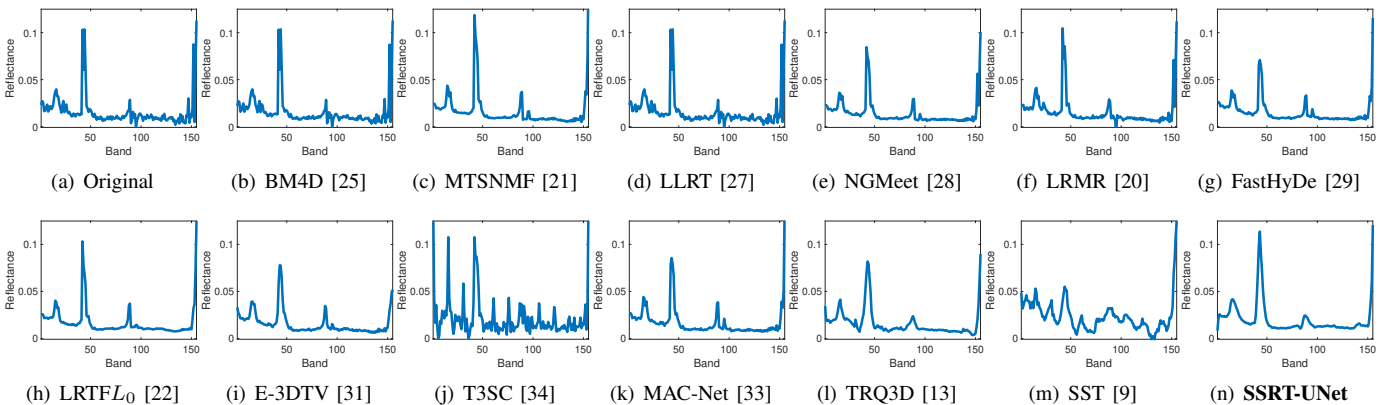


Fig. 9. Reflectance of pixel (246,278) in the GF-5 Wuhan HSI.

to better reflect spectral correlations and differences allows E-3DTV to outperform TRQ3D, which introduces RNNs to model incomplete spectral correlations in the HSI, especially when the Pavia City Center HSI has different spectral features from the training data. Exploiting long-range correlations in spectral and spatial dimensions, transformer-based SST shows better performance than TRQ3D. However, it still struggles when dealing with testing data with a different number of bands. Our SSUMamba achieves the best performance in the Pavia City Center HSI by exploiting complete global spatial-spectral correlations with SSM.

Fig. 6 shows the false-color images recovered by all compared methods. The model-based methods, designed for Gaussian noise, fail to eliminate artifacts such as stripes and artifacts in the mixture noise. E-3DTV, which models the low-rankness of the spatial and spectral gradient map in HSI, achieves the best performance in the mixture noise. However, it still gets blurred due to the limited modeling ability in spatial. Transformer-based methods, such as TRQ3D and SST, exhibit some degree of failure in Pavia City Center HSI reconstruction due to spectral variations between the Pavia City Center HSI and the training set ICVL. Our SSUMamba, which captures global spatial-spectral correlations effectively, yields highly accurate reconstructions with minimal artifacts, particularly in cases with heavy noise, where detailed information degrades.

Fig. 7 shows the spectral reflectances of the mixture noise. The proposed SSUMamba effectively exploits global spatial-spectral correlations to recover the spectral reflectance, resulting in the best match with the clean HSI among all methods.

C. Comparison on Real-World HSIs

We carried out extra experiments on real-world remote-sensing HSIs to thoroughly evaluate the effectiveness of denoising across various methods. We provide a qualitative comparative analysis to assess the denoising results.

1) *Gaofen-5 Wuhan HSI*: The Gaofen-5 (GF-5) Wuhan HSI was acquired using the Advanced Hyperspectral Imager (AHSI) with a resolution of 300×300 pixels and 155 spectral bands. In our real-world experiment, we applied all compared methods to the original noisy HSI. The results are presented in Fig. 8, where the original image is degraded by impulse and stripes. Among model-based methods, FastHyDe and LRTFL₀ achieved better performance thanks to their ability to recover from mixture noise. T3SC and MAC-Net effectively removed most of the stripes in the GF-5 Wuhan HSI. T3SC produced sharper results by learning both spectral and spatial information in a trainable sparse coding model. However, Transformer-based TRQ3D and SST failed to completely remove all the stripes due to limited adaptability to the imaging environment. Our SSUMamba method, which effectively captures global

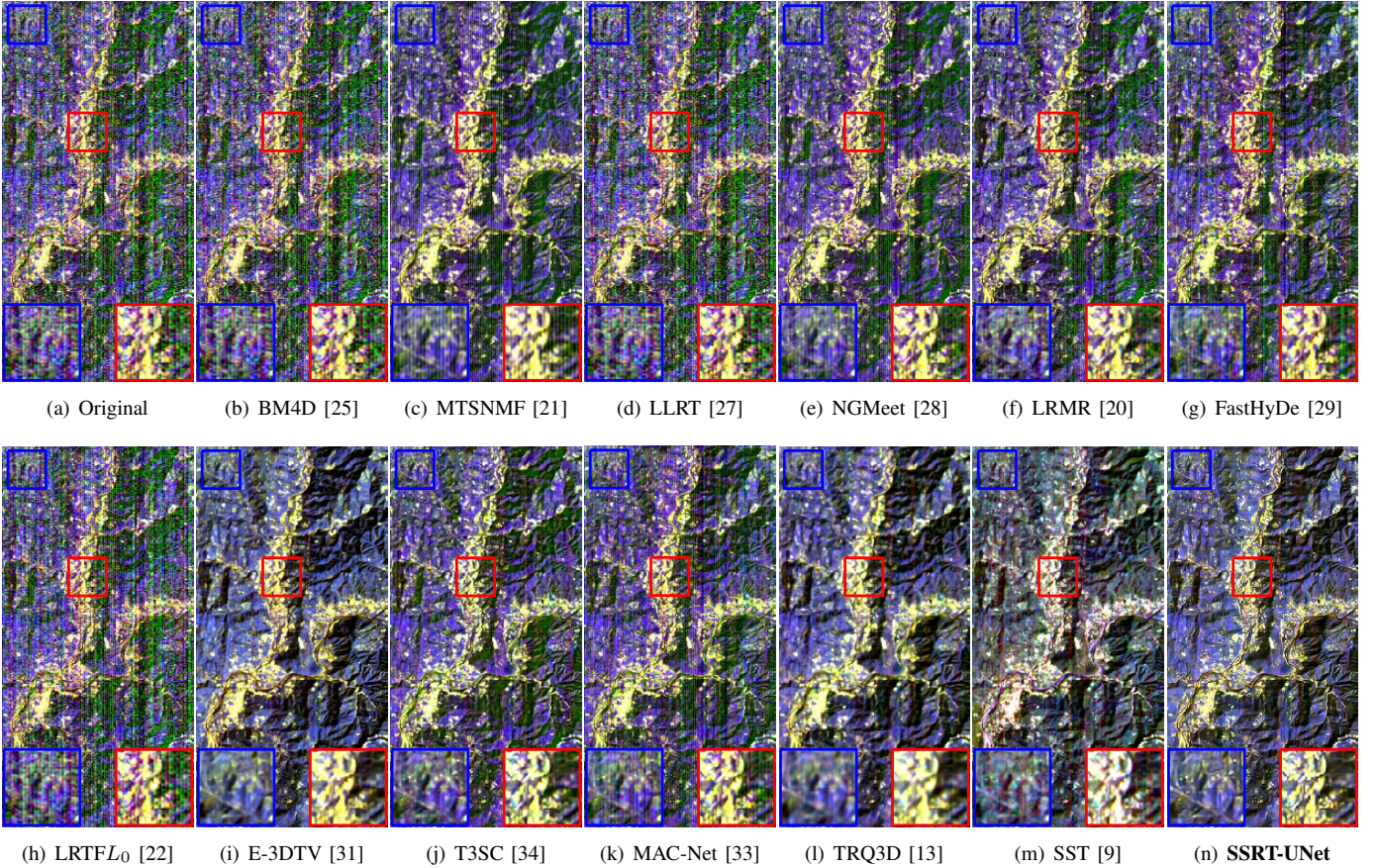


Fig. 10. Denoising results on the EO-1 HSI. The false-color images are generated by combining bands 163,132, and 30.

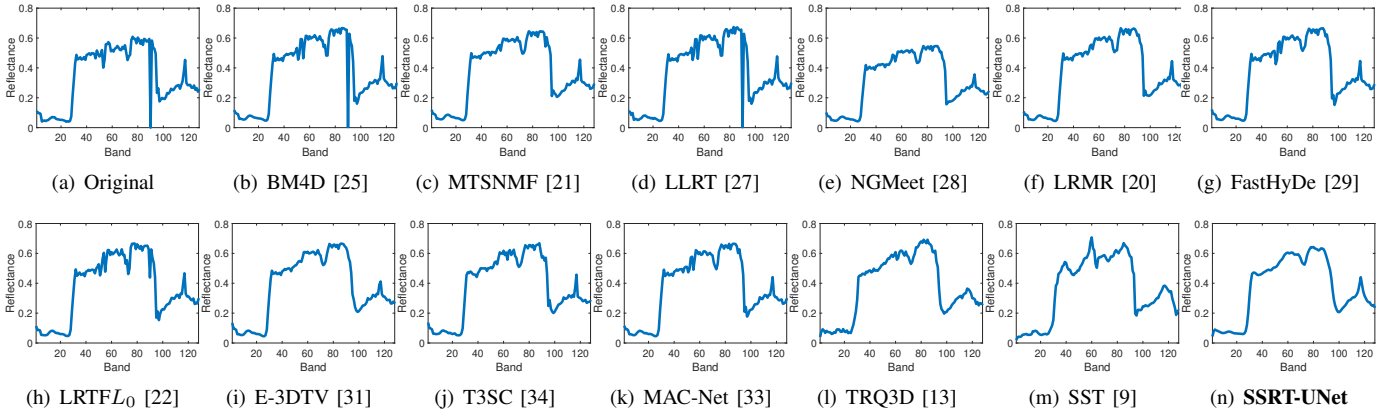


Fig. 11. Reflectance of pixel (151,125) in the EO-1 HSI.

spatial-spectral correlations to learn the deep 3-D features of the HSI, yielded highly accurate reconstructions with minimal artifacts and sharper edges compared to all other methods.

Spectral reflectances are depicted in Fig. 7. The heavy impulse and stripes cause significant spectral distortion, as seen in Fig. 9(a). T3SC and SST process the HSI in patches, leading to incomplete global spatial-spectral correlations and spectral jitters. In contrast, our SSUMamba, which captures global spatial-spectral correlations effectively, can recover spectral reflectance more accurately, resulting in smoother curves that closely resemble the original shape.

2) *Earth Observing-1 HSI*: The Earth Observing-1 (EO-1) HSI was acquired by Hyperion with 242 bands and a

resolution of 1000×400 pixels. Following [20], the water absorption bands were removed, and the final HSI was cropped to 400×200 pixels with 166 bands. Similar to the experiment with the GF-5 Wuhan HSI, we applied all compared methods to the original noisy HSI. The results are presented in Fig. 10. The presence of heavier impulse and stripe noise makes the denoising task more challenging. Besides E-3DTV, all other model-based methods failed to effectively remove the stripes and impulse noise due to the heavier noise. Although E-3DTV removed the stripes and impulse noise, it resulted in blurred edges. Among deep learning-based methods, T3SC and TRQ3D successfully removed most of the stripes. However, insufficient modeling of global spatial-

spectral correlations resulted in blurring similar to E-3DTV. MAC-Net and SST were unable to remove all the stripes, while SST introduced color distortion. Our SSUMamba effectively learned the deep 3-D nature of the HSI, incorporating spatial and spectral information to produce sharper edges and more accurate colors. Spectral reflectances are shown in Fig. 11, where jitters and discontinuities are evident in Fig. 11(a). SSUMamba achieved smoother and more continuous spectral reflectance, closer to the clean HSI.

D. Ablation Study

In this section, we present the performance of SSUMamba with varying widths to illustrate its performance under different number of parameters. Additionally, we conduct ablation experiments on different modules to demonstrate their individual contributions to performance.

TABLE IV
ABLATION STUDY ON THE EFFECT OF INTRODUCED COMPONENTS.

SSAS	Bidirectional	PSNR \uparrow	SSIM \uparrow	SAM \downarrow
✓	✓	34.55	.9444	.1047
✗	✓	34.40	.9444	.1056
✓	✗	34.26	.9417	.1086

1) *Effectiveness of Different Modules*: We assess the efficacy of the components introduced in SSUMamba, which include the SSAS and bidirectional Mamba. The model was trained on the ICVL training set and tested on the Houston 2018 HSI dataset with mixed noise. The results are presented in Table IV. The model lacking SSAS will consistently scan the HSI with a fixed priority, $W \rightarrow H \rightarrow B$. Incorporating SSAS does not introduce additional parameters or computational complexity; rather, it aids the model in exploiting information flows the 3-D nature of the HSI data in all directions. This enhancement is reflected in improved PSNR, SAM, and nearly identical SSIM results. Furthermore, the introduction of the bidirectional Mamba further refines the global spatial-spectral correlation modeling, resulting in enhanced performance across all metrics.

2) *Effect of Width*: We further investigate the effectiveness of network width in our SSUMamba framework. To assess the impact of network width on performance, we conducted experiments with varying numbers of channels, which play a pivotal role in the network width. In the 6 SSAS Mamba blocks, the channel configuration is set as $[BC, BC \times 2, BC \times 2, BC \times 4, BC \times 4, BC \times 8]$, where BC means base channels. We compare the performance of SSUMamba with different numbers of base channels, including 32, 24, 16, and 12. We also compare the results with transformer-based methods, TRQ3D and SST. The model was trained on the ICVL training set and tested on the Houston 2018 HSI dataset with mixed noise. The results are presented in Table V. As we can see, the performance of our proposed SSUMamba continues to extend as the width is enhanced. Compared with transformer-based methods, which suffer from the $O(n^2)$ complexity, our SSUMamba achieves better performance with fewer parameters and lower memory consumption. This is achieved thanks

to the linear complexity facilitated by SSM and global spatial-spectral correlation modeling in our SSAS Mamba block.

TABLE V
STUDY ON THE IMPACT OF NETWORK WIDTH (CHANNELS).

Channels	#Param.	Memory	PSNR \uparrow	SSIM \uparrow	SAM \downarrow
32	10.4M	1,802M	34.55	.9444	.1047
24	5.9M	1,386M	34.41	.9413	.1054
16	2.6M	991M	33.72	.9373	.1128
12	1.5M	785M	33.39	.9287	.1174
Methods	#Param.	Memory	PSNR \uparrow	SSIM \uparrow	SAM \downarrow
TRQ3D	0.68M	675M	32.55	.9194	.1241
SST	4.14M	1,600M	31.07	.9166	.1390

V. CONCLUSION

This paper introduces a SSUMamba for HSI denoising. We incorporate the SSM with linear complexity to enable global spatial-spectral correlation modeling in HSIs. By utilizing the Spatial-Spectral Alternating Scan Mamba block, our SSUMamba can effectively exploit the information flow in all directions in the HSI data and enhance the 3-D characteristic. Experimental results with compared methods demonstrate that our proposed method achieves state-of-the-art performance. The ablation study further validates the effectiveness of the introduced components.

REFERENCES

- [1] B. Thai and G. Healey, "Invariant subpixel material detection in hyperspectral imagery," *IEEE Trans. Geosci. Remote Sens.*, vol. 40, no. 3, pp. 599–608, 2002.
- [2] X. Yang, B. Tu, Q. Li, J. Li, and A. Plaza, "Graph evolution-based vertex extraction for hyperspectral anomaly detection," *IEEE Trans. Neural Netw. Learn. Syst.*, pp. 1–15, 2023.
- [3] L. Gao, X. Sun, X. Sun, L. Zhuang, Q. Du, and B. Zhang, "Hyperspectral anomaly detection based on chessboard topology," *IEEE Trans. Geosci. Remote Sens.*, vol. 61, pp. 1–16, 2023.
- [4] W. Dong, J. Zhao, J. Qu, S. Xiao, N. Li, S. Hou, and Y. Li, "Abundance matrix correlation analysis network based on hierarchical multihead self-cross-hybrid attention for hyperspectral change detection," *IEEE Trans Geosci Remote Sens.*, vol. 61, pp. 1–13, 2023.
- [5] F. Xiong, J. Zhou, and Y. Qian, "Material based object tracking in hyperspectral videos," *IEEE Trans. Image Process.*, vol. 29, pp. 3719–3733, 2020.
- [6] Z. Li, F. Xiong, J. Zhou, J. Lu, and Y. Qian, "Learning a deep ensemble network with band importance for hyperspectral object tracking," *IEEE Trans. Image Process.*, vol. 32, pp. 2901–2914, 2023.
- [7] F. Luo, T. Zhou, J. Liu, T. Guo, X. Gong, and J. Ren, "Multiscale diff-changed feature fusion network for hyperspectral image change detection," *IEEE Trans. Geosci. Remote Sens.*, vol. 61, pp. 1–13, 2023.
- [8] N. Li, S. Jiang, J. Xue, S. Ye, and S. Jia, "Texture-aware self-attention model for hyperspectral tree species classification," *IEEE Trans. Geosci. Remote Sens.*, vol. 62, pp. 1–15, 2024.
- [9] M. Li, Y. Fu, and Y. Zhang, "Spatial-spectral transformer for hyperspectral image denoising," in *Proc. AAAI Conf. Artif. Intell. (AAAI)*, 2023.
- [10] G. Fu, F. Xiong, J. Lu, J. Zhou, J. Zhou, and Y. Qian, "Hyperspectral image denoising via spatial-spectral recurrent transformer," *IEEE Trans. Geosci. Remote Sens.*, vol. 62, pp. 1–14, 2024.
- [11] K. Wei, Y. Fu, and H. Huang, "3-D quasi-recurrent neural network for hyperspectral image denoising," *IEEE Trans. Neural Netw. Learn. Syst.*, vol. 32, no. 1, pp. 363–375, 2021.
- [12] X. Fu, Y. Guo, M. Xu, and S. Jia, "Hyperspectral image denoising via robust subspace estimation and group sparsity constraint," *IEEE Trans. Geosci. Remote Sens.*, vol. 61, pp. 1–16, 2023.
- [13] L. Pang, W. Gu, and X. Cao, "TRQ3DNet: A 3D quasi-recurrent and transformer based network for hyperspectral image denoising," *Remote Sensing*, vol. 14, no. 18, 2022.
- [14] A. Gu and T. Dao, "Mamba: Linear-time sequence modeling with selective state spaces," *arXiv preprint arXiv:2312.00752*, 2023.

- [15] A. Gu, K. Goel, and C. Re, "Efficiently modeling long sequences with structured state spaces," in *International Conference on Learning Representations (ICLR)*, 2022.
- [16] Y. Liu, Y. Tian, Y. Zhao, H. Yu, L. Xie, Y. Wang, Q. Ye, and Y. Liu, "Vmamba: Visual state space model," *arXiv preprint arXiv:2401.10166*, 2024.
- [17] K. Li, X. Li, Y. Wang, Y. He, Y. Wang, L. Wang, and Y. Qiao, "Videomamba: State space model for efficient video understanding," *arXiv preprint arXiv:2403.06977*, 2024.
- [18] Y. Liu, J. Xiao, Y. Guo, P. Jiang, H. Yang, and F. Wang, "Hsidmamba: Exploring bidirectional state-space models for hyperspectral denoising," *arXiv preprint arXiv:2404.09697*, 2024.
- [19] N. Liu, W. Li, Y. Wang, R. Tao, Q. Du, and J. Chanussot, "A survey on hyperspectral image restoration: From the view of low-rank tensor approximation," *Science China Information Sciences*, vol. 66, no. 4, p. 140302, 2023.
- [20] H. Zhang, W. He, L. Zhang, H. Shen, and Q. Yuan, "Hyperspectral image restoration using low-rank matrix recovery," *IEEE Trans. Geosci. Remote Sens.*, vol. 52, no. 8, pp. 4729–4743, 2014.
- [21] M. Ye, Y. Qian, and J. Zhou, "Multitask sparse nonnegative matrix factorization for joint spectral-spatial hyperspectral imagery denoising," *IEEE Trans. Geosci. Remote Sens.*, vol. 53, no. 5, pp. 2621–2639, 2014.
- [22] F. Xiong, J. Zhou, and Y. Qian, "Hyperspectral restoration via L_0 gradient regularized low-rank tensor factorization," *IEEE Trans. Geosci. Remote Sens.*, vol. 57, no. 12, pp. 10 410–10 425, 2019.
- [23] Z. Zha, B. Wen, X. Yuan, J. Zhang, J. Zhou, Y. Lu, and C. Zhu, "Nonlocal structured sparsity regularization modeling for hyperspectral image denoising," *IEEE Trans. Geosci. Remote Sens.*, vol. 61, pp. 1–16, 2023.
- [24] X. Su, Z. Zhang, and F. Yang, "Fast hyperspectral image denoising and destriping method based on graph laplacian regularization," *IEEE Trans. Geosci. Remote Sens.*, vol. 61, pp. 1–14, 2023.
- [25] M. Maggioni, V. Katkovnik, K. Egiazarian, and A. Foi, "Nonlocal transform-domain filter for volumetric data denoising and reconstruction," *IEEE Trans. Image Process.*, vol. 22, no. 1, pp. 119–133, 2012.
- [26] Y. Peng, D. Meng, Z. Xu, C. Gao, Y. Yang, and B. Zhang, "Decomposable nonlocal tensor dictionary learning for multispectral image denoising," in *Proc. IEEE Conf. Comput. Vis. Pattern Recognit. (CVPR)*, 2014, pp. 2949–2956.
- [27] Y. Chang, L. Yan, and S. Zhong, "Hyper-Laplacian regularized unidirectional low-rank tensor recovery for multispectral image denoising," in *Proc. IEEE Conf. Comput. Vis. Pattern Recognit. (CVPR)*, 2017, pp. 5901–5909.
- [28] W. He, Q. Yao, C. Li, N. Yokoya, Q. Zhao, H. Zhang, and L. Zhang, "Non-local meets global: An iterative paradigm for hyperspectral image restoration," *IEEE Trans. Pattern Anal. Mach. Intell.*, vol. 44, no. 4, pp. 2089–2107, 2022.
- [29] L. Zhuang and J. M. Bioucas-Dias, "Fast hyperspectral image denoising and inpainting based on low-rank and sparse representations," *IEEE J. Sel. Topics Appl. Earth Observations Remote Sens.*, vol. 11, no. 3, pp. 730–742, 2018.
- [30] Y. Chen, W. Cao, L. Pang, J. Peng, and X. Cao, "Hyperspectral image denoising via texture-preserved total variation regularizer," *IEEE Trans. Geosci. Remote Sens.*, vol. 61, pp. 1–14, 2023.
- [31] J. Peng, Q. Xie, Q. Zhao, Y. Wang, L. Yee, and D. Meng, "Enhanced 3DTV regularization and its applications on HSI denoising and compressed sensing," *IEEE Trans. Image Process.*, vol. 29, pp. 7889–7903, 2020.
- [32] H. Zhang, T.-Z. Huang, X.-L. Zhao, W. He, J. K. Choi, and Y.-B. Zheng, "Hyperspectral image denoising: Reconciling sparse and low-tensor-ring-rank priors in the transformed domain," *IEEE Trans. Geosci. Remote Sens.*, vol. 61, pp. 1–13, 2023.
- [33] F. Xiong, J. Zhou, Q. Zhao, J. Lu, and Y. Qian, "MAC-Net: Model-aided nonlocal neural network for hyperspectral image denoising," *IEEE Trans. Geosci. Remote Sens.*, vol. 60, pp. 1–14, 2022.
- [34] T. Bodrito, A. Zouaoui, J. Chanussot, and J. Mairal, "A trainable spectral-spatial sparse coding model for hyperspectral image restoration," in *Proc. Adv. Neural Inf. Process. Syst. (NeurIPS)*, vol. 34, 2021, pp. 5430–5442.
- [35] K. Zhang, W. Zuo, Y. Chen, D. Meng, and L. Zhang, "Beyond a Gaussian denoiser: Residual learning of deep CNN for image denoising," *IEEE Trans. Image Process.*, vol. 26, no. 7, pp. 3142–3155, 2017.
- [36] A. Maffei, J. M. Haut, M. E. Paoletti, J. Plaza, L. Bruzzone, and A. Plaza, "A single model CNN for hyperspectral image denoising," *IEEE Trans. Geosci. Remote Sens.*, vol. 58, no. 4, pp. 2516–2529, 2020.
- [37] W. Liu and J. Lee, "A 3-D atrous convolution neural network for hyperspectral image denoising," *IEEE Trans. Geosci. Remote Sens.*, vol. 57, no. 8, pp. 5701–5715, 2019.
- [38] W. Dong, H. Wang, F. Wu, G. Shi, and X. Li, "Deep spatial-spectral representation learning for hyperspectral image denoising," *IEEE Transactions on Computational Imaging*, vol. 5, no. 4, pp. 635–648, 2019.
- [39] G. Fu, F. Xiong, J. Lu, J. Zhou, and Y. Qian, "Nonlocal spatial-spectral neural network for hyperspectral image denoising," *IEEE Trans. Geosci. Remote Sens.*, vol. 60, pp. 1–16, 2022.
- [40] D. Hong, Z. Han, J. Yao, L. Gao, B. Zhang, A. Plaza, and J. Chanussot, "Spectralformer: Rethinking hyperspectral image classification with transformers," *IEEE Trans. Geosci. Remote Sens.*, vol. 60, pp. 1–15, 2022.
- [41] S. Zhang, J. Zhang, X. Wang, J. Wang, and Z. Wu, "ELS2T: Efficient lightweight spectral-spatial transformer for hyperspectral image classification," *IEEE Trans. Geosci. Remote Sens.*, 2023.
- [42] H. Yu, Z. Xu, K. Zheng, D. Hong, H. Yang, and M. Song, "MSTNet: A multilevel spectral-spatial transformer network for hyperspectral image classification," *IEEE Trans. Geosci. Remote Sens.*, vol. 60, pp. 1–13, 2022.
- [43] H. Yang, H. Yu, K. Zheng, J. Hu, T. Tao, and Q. Zhang, "Hyperspectral image classification based on interactive transformer and cnn with multilevel feature fusion network," *IEEE Geosci. Remote Sens. Lett.*, vol. 20, pp. 1–5, 2023.
- [44] M. Jiang, Y. Su, L. Gao, A. Plaza, X.-L. Zhao, X. Sun, and G. Liu, "GraphGST: Graph generative structure-aware transformer for hyperspectral image classification," *IEEE Trans. Geosci. Remote Sens.*, vol. 62, pp. 1–16, 2024.
- [45] F. Wang, J. Li, Q. Yuan, and L. Zhang, "Local-global feature-aware transformer based residual network for hyperspectral image denoising," *IEEE Trans. Geosci. Remote Sens.*, vol. 60, pp. 1–19, 2022.
- [46] M. Li, J. Liu, Y. Fu, Y. Zhang, and D. Dou, "Spectral enhanced rectangle transformer for hyperspectral image denoising," in *Proc. IEEE Conf. Comput. Vis. Pattern Recognit. (CVPR)*, June 2023, pp. 5805–5814.
- [47] L. Chen, G. Vivone, J. Qin, J. Chanussot, and X. Yang, "Spectral-spatial transformer for hyperspectral image sharpening," *IEEE Trans. Neural Netw. Learn. Syst.*, 2023.
- [48] Z. Liu, J. Ning, Y. Cao, Y. Wei, Z. Zhang, S. Lin, and H. Hu, "Video swin transformer," in *Proc. IEEE Conf. Comput. Vis. Pattern Recognit. (CVPR)*, 2022, pp. 3202–3211.
- [49] J. He, L. Zhao, H. Yang, M. Zhang, and W. Li, "HSI-BERT: Hyperspectral image classification using the bidirectional encoder representation from transformers," *IEEE Trans. Geosci. Remote Sens.*, vol. 58, no. 1, pp. 165–178, 2020.
- [50] L. Zhu, B. Liao, Q. Zhang, X. Wang, W. Liu, and X. Wang, "Vision mamba: Efficient visual representation learning with bidirectional state space model," *arXiv preprint arXiv:2401.09417*, 2024.
- [51] G. Chen, Y. Huang, J. Xu, B. Pei, Z. Chen, Z. Li, J. Wang, K. Li, T. Lu, and L. Wang, "Video mamba suite: State space model as a versatile alternative for video understanding," *arXiv preprint arXiv:2403.09626*, 2024.
- [52] J. Ma, F. Li, and B. Wang, "U-mamba: Enhancing long-range dependency for biomedical image segmentation," *arXiv preprint arXiv:2401.04722*, 2024.
- [53] Y. Shi, B. Xia, X. Jin, X. Wang, T. Zhao, X. Xia, X. Xiao, and W. Yang, "VmambaR: Visual state space model for image restoration," *arXiv preprint arXiv:2403.11423*, 2024.
- [54] J. X. Yang, J. Zhou, J. Wang, H. Tian, and A. W. C. Liew, "Hsimamba: Hyperspectral imaging efficient feature learning with bidirectional state space for classification," *arXiv preprint arXiv:2404.00272*, 2024.
- [55] J. Yao, D. Hong, C. Li, and J. Chanussot, "Spectralmamba: Efficient mamba for hyperspectral image classification," *arXiv preprint arXiv:2404.08489*, 2024.
- [56] Y. Chen, X. Cao, Q. Zhao, D. Meng, and Z. Xu, "Denoising hyperspectral image with non-i.i.d. noise structure," *IEEE Trans. Cybern.*, vol. 48, no. 3, pp. 1054–1066, 2018.
- [57] W. He, H. Zhang, L. Zhang, and H. Shen, "Hyperspectral image denoising via noise-adjusted iterative low-rank matrix approximation," *IEEE J. Sel. Topics Appl. Earth Observ. Remote Sens.*, vol. 8, no. 6, pp. 3050–3061, 2015.